Surface pressure visualization by 3D PTV

Jux, Constantin; Sciacchitano, Andrea; Scarano, Fulvio

DOI
10.3929/ethz-b-000279192

Publication date
2018

Document Version
Final published version

Published in
Proceedings 18th International Symposium on Flow Visualization

SURFACE PRESSURE VISUALIZATION BY 3D PTV

C. Jux[1,c], A. Sciacchitano[1], F. Scarano[1]

[1] Faculty of Aerospace Engineering, TU Delft, 2629 HS Delft, The Netherlands
[c] Corresponding author: Tel.: +49 162 69 20 198; Email: C.Jux@tudelft.nl

KEYWORDS:
Main subjects: Surface pressure visualization, Large-scale 3D PTV
Fluid: Low speed flows, Aerodynamics
Visualization method(s): Coaxial volumetric velocimetry, Robotic volumetric PIV
Other keywords: Cycling aerodynamics, Large-scale PIV, Bluff body flows, 3D PTV

ABSTRACT: *Some recent trends in the development of PIV techniques are leading to the realization of velocity measurement at large scale. Moreover, methods for evaluating the fluid flow pressure from PIV data have been successfully demonstrated at small scale and for simple geometries. Methods for quantitative visualization of surface flow properties such as skin-friction and pressure are comparatively less developed, despite the great interest for the aerodynamic insight they provide for the study of the flow around 3D complex objects.*
The accuracy of the pressure evaluation at the surface is inquired in this work by dedicated measurements over a sphere at $Re_d = 8 \times 10^4$. The measurements made with robotic PIV are compared to direct surface pressure measurements. The solution of the Reynolds averaged momentum equations is performed with the Poisson problem formulation and the results are compared with potential flow theory and some simplified models. The accuracy of stagnation pressure depends upon the measurement resolution. Instead, the suction peak region is generally underestimated. The pressure in the separated region is retrieved with sufficient accuracy.
The surface flow properties visualization of a time-trialing full-scale cyclist replica at 14 m/s ($Re = 5.5 \times 10^5$) is performed as a demonstration of the above method to a complex 3D problem at large scale. The data obtained with the robotic PIV technique is analyzed in close proximity of the solid surface and the skin friction lines of the time averaged velocity field are inspected. The topological analysis of the skin friction lines yields clearly the evolution of the flow around the body segments returning the details of the separated flow regions and local recirculation zones. The analysis of the surface pressure distribution yields results in accordance with the skin-friction lines, the outer flow velocity field as well as the vortex topology.

1 Introduction

The recent introduction of coaxial volumetric velocimetry (CVV) by Schneiders et al. (2018) [16] has given impetus to three dimensional velocity field measurements around large and complex geometries of relevance for many fields of aerodynamics. The authors (Jux et al. 2018) [8] have coupled CVV with a robotic manipulation system to realize volumetric PTV measurements around a full-scale cyclist model. The measurements rely upon Helium filled soap bubbles (HFSB) [14] as flow tracers known for their high scattering intensity. The introduction of these three technologies, namely HFSB, CVV and robotic volumetric PIV are motivated by the desire of acquiring volumetric airflow measurements on a large scale. The trend towards such large-scale volumetric PIV studies is recognized in a number of recent studies such as in the work of Caridi et al. (2016) [4] on the tip vortex of a vertical axis wind turbine (measurement volume, V = 40×20×15 cm^3), that of Rius Vidales (2016) [13] on the bi-stable wake structure of a frigate ship model (V = 45×25×11 cm^3), the cyclist wake analysis of Sciacchitano et al. (2018) [19] (V = 162×100×5 cm^3) or the robotic volumetric PIV study of Martínez Gallar et al. (2018) [9] on the wake flow of a flapping-wing micro air vehicle (V = 50×40×30 cm^3).

The studies mentioned above demonstrated the feasibility of large-scale volumetric velocity field measurements. A second trend in PIV developments is the evaluation of pressure from (3D) PIV data

as highlighted in a review by van Oudheusden (2013) [10]. The tomographic PIV study of Schneiders et al. (2016) [17] on the flow downstream of a truncated cylinder is the first study that reports the use of large-scale (i.e. using HFSB as tracers) volumetric PIV to determine the flow field pressure. The study, is limited to the analysis of the pressure close to the flat plate downstream of the cylinder and excellent agreement is reported for the time-averaged pressure with respect to pressure taps.

The evaluation of the flow field pressure over the curved surface of an airfoil has been addressed in the works of Ragni and coauthors (Ragni et al. 2009, 2012) [11, 12], however, with planar PIV. The results indicated that a good accuracy can be achieved in general, provided that the measurements are performed at good spatial resolution. A pronounced discrepancy in regions with strong local curvature and gradient of pressure was ascribed to insufficient spatial resolution.

Volumetric robotic PIV typically offers lower spatial resolution than the typical measurements with the planar technique. Nonetheless, volumetric measurements allow to map the velocity field over complex surfaces, which makes it interesting for applications in the aerodynamic study of 3D objects such as for instance in sports.

One of the limitations of pressure evaluation from velocity data arises from the spatial resolution limited by the data density. Typically PIV/PTV measurements are spatially averaged over a small volume, which corresponds to the cross-correlation window in PIV and to the three-dimensional bin employed for the computation of the velocity statistics in 3D PTV. The distance between adjacent velocity vectors is typically a fraction (25% to 100%) of the volume linear dimension l_V. Consequently, any measured spatial gradient suffers from filtering effects. Furthermore, the limited spatial resolution, imposes a finite distance from the solid surface, thus complicating the evaluation of the flow field variables at the surface. The present work addresses the latter issue and discusses options to evaluate the surface-pressure on solid objects based on the near flow velocity field.

The proposed methods of surface pressure evaluation from PIV data can be categorized in three types: purely mathematical models which extrapolate the field pressure to the surface, physical models which leverage knowledge of the flow behavior, and hybrid models which impose some physical constraints in a mathematical mapping model.

The theoretical discussion is accompanied by two wind tunnel experiments to validate the findings and to demonstrate the potential of the presented methodology in large-scale aerodynamic experiments.

2 Methods

The basic principles of robotic volumetric PIV are summarized hereafter, before addressing the procedures of evaluating pressure in the field and on an object surface in Sec. 2.3.

2.1 Principles of robotic volumetric PIV

Details on the working principles of robotic volumetric PIV can be found in the work of Jux et al. (2018) [8]. The technique utilizes the compactness of coaxial volumetric velocimetry (Schneiders et al. 2018 [16]), a low tomographic aperture imaging system which greatly enhances optical access in volumetric PIV approaches by aligning imaging and illumination direction and which lends itself well to robotic manipulation. The CVV system requires a calibration at start of measurement, consisting of a pinhole model calibration (Soloff et al. 1997 [20]) and a volume self-calibration (Wieneke 2008 [23]). Subsequently, the CVV probe can be manipulated by a robotic arm, allowing for rapid acquisitions of time-averaged flow field data by a volume scanning approach.

2.2 Data Acquisition and Velocity Field Evaluation

In the selected robotic volumetric PIV approach images are acquired in a continuous, time-resolved manner. Typically raw CVV images are pre-processed by a temporal frequency filter, e.g. a high pass frequency filter as presented by Sciacchitano and Scarano (2014) [18], which eliminates background noise and light reflections on the test model. Subsequently, advantage of the time-resolved PIV images is drawn by means of computationally efficient Lagrangian particle tracking. In specific, the Shake-the-Box (STB) algorithm (Schanz et al. 2016 [15]) is utilized for particle tracking, providing information on particle location, velocity and accelerations. The unstructured particle data is mapped onto a structured grid by means of temporal and spatial averaging: Gaussian averaging is performed within cubic cells of finite size (typically on the order of a few millimeters) which span the full measurement domain. The time-averaged velocity data on the structured grid can subsequently be analyzed further, e.g. for the extraction of the pressure field.

2.3 Pressure field evaluation

The evaluation of the 3D time-averaged pressure field may be split into two main steps: first, the evaluation of the static pressure in the field, and second, the pressure mapping onto the object surface. Decisive factors which are discussed include the treatment of boundary conditions, the effect of spatial resolution and discretization of both, fluid measurement domain and object surface.

2.3.1 Field pressure

The mean pressure gradient in the interior measurement domain is evaluated through application of the Poisson approach to the Reynolds averaged momentum equation, (e.g. van Oudheusden, 2013 [10])

$$\nabla^2 \overline{p} = -\rho \nabla \cdot (\overline{\boldsymbol{u}} \cdot \nabla)\overline{\boldsymbol{u}} - \rho \nabla \cdot \nabla \cdot \left(\overline{\boldsymbol{u}'\boldsymbol{u}'}\right) \qquad (1)$$

The velocity gradients on the right hand side are computed from the time-averaged flow field by second order central differences on the interior domain. Along the boundaries single-sided first order difference schemes are used instead. The Laplace operator is discretized by means of second order central differences too. At the boundaries, the von Neumann condition is applied as proposed in the work of Ebbers and Farnebäck (2009) [6].

Application of the von Neumann boundary condition will yield the solution of the pressure field up to a finite integration constant. To eliminate the latter, a Dirichlet condition is to be specified at a known reference location. For the presented data, the pressure far upstream of the test object is matched to the expected free-stream pressure.

2.3.2 Surface pressure

The evaluation of surface pressure from 3D PTV data is a non-trivial problem. As a result of spatially averaging scattered particle data in finite cells, the recorded velocity field obeys a finite spatial resolution. This creates two stumbling blocks in the evaluation of surface pressure from PIV data: first, representations of spatial gradients in the flow suffer from truncation errors. Second, due to the finite spatial resolution any velocity measurement features a finite distance to any object surface. The recent work of Faleiros et al. (2018) [7] shows that HFSB tracers are well suitable to resolve turbulent wall-boundary layers with sub-millimeter spatial resolution in a planar PIV measurement, yet the typical resolution reported for CVV measurements is on the order of 10 mm and therefore it is insufficient to resolve boundary layers of typical flows of interest. Consequently, a model is required which bridges the gap between the field pressure measured by volumetric PIV and the desired surface pressure.

Options for surface pressure evaluation from PIV data range from purely mathematical to highly physical models: the work of Ragni et al. (2009) [11] suggests that in a planar measurement a linear extrapolation of pressure data to the surface is sufficient to recover loads on a transonic airfoil. In general terms, a mathematical extrapolation of the field pressure to the surface can be realized where the uncertainty of the surface pressure prediction is expected to reduce with increasing spatial resolution.

Rather than a fully mathematical extrapolation, one may impose some physical constraints within an extrapolation model. For instance, applying a von Neumann condition on the object surface, the pressure gradient in the wall-normal direction ($\partial p/\partial \vec{n}$) can be set to zero. The pressure gradient along the same direction can also be inferred from the nearby field measurements. This allows already for a quadratic interpolation of the pressure to the surface, taking the information of pressure and pressure gradient at a nearby measurement point (x_c) and imposing the von Neumann condition at the surface point (x_s).

$$p(x_c) = p_c \qquad \frac{\partial p(x_c)}{\partial n} = \frac{\partial p_c}{\partial n} \qquad \frac{\partial p(x_s)}{\partial n} = 0 \tag{2}$$

Instead of mathematical models, physics based models can be envisaged. Imposing the no-slip condition, the flow needs to come to rest at an object surface. The stagnation of the wall-normal flow component of a nearby PIV measurement ($\vec{u} \cdot \vec{n}$) will cause a finite pressure difference Δp, which in the assumption that Bernoulli's principle is valid along the wall-normal direction considering only the wall-normal velocity component, reads

$$\Delta p = \frac{1}{2}\rho(\vec{u} \cdot \vec{n})^2 \tag{3}$$

Subsequently the pressure at a surface point x_s can be expressed as the sum of the pressure value at a measurement point x_c and the pressure difference Δp,

$$p(x_s) = p(x_c) + \Delta p \tag{4}$$

A schematic illustration of this 'stagnation approach' is given in Fig. 1.

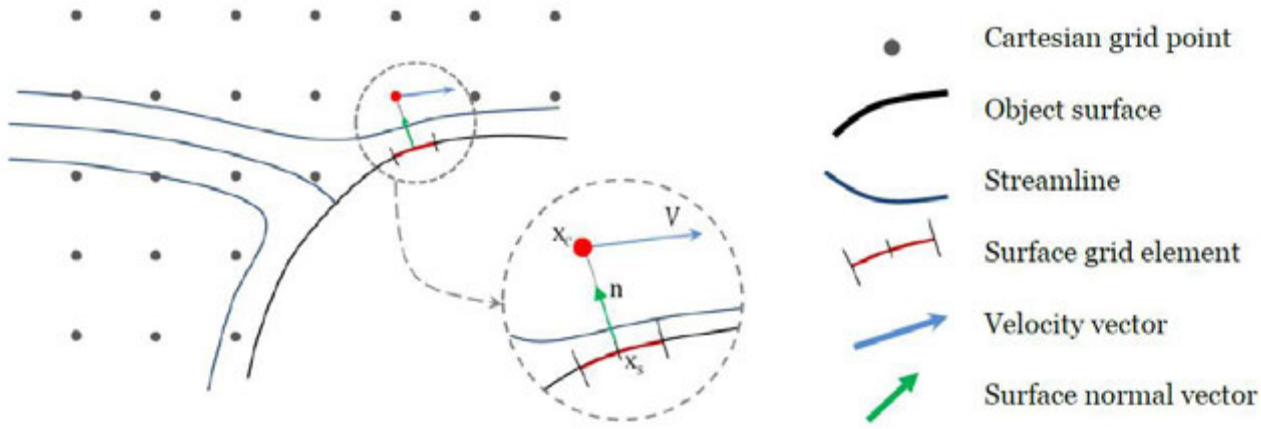

Fig. 1 Schematic illustration of the stagnation pressure mapping approach, using velocity information from the Cartesian measurement grid (x_c) to evaluate the surface pressure at a grid element (x_s).

The three proposed methods, namely the linear extrapolation, the quadratic interpolation using the von Neumann boundary condition, and the stagnation model approach are compared for the case of the pressure distribution on a sphere in Sec. 4.1.

3 Wind tunnel experiments

The experimental data presented in this work is conducted in the Open Jet Facility (OJF) wind tunnel at TU Delft. The atmospheric, open-jet wind tunnel features a contraction of 3:1 with an octagonal nozzle exit of 2.85 × 2.85 m^2. The turbulence intensity of the wind tunnel is below 1% for operations in the nominal wind speed range of 4 to 35 m/s.

Helium filled soap bubbles serve as high contrast seeding particles which are introduced into the flow at the contraction exit. Two aerodynamic rakes, housing 80 respectively 200 individual HFSB generators are used for the experimental campaigns. Specifications of the seeding systems are given in Tab. 1. The generators are operated through a fluid supply unit (FSU) controlling the pressures of air, helium and soap. The turbulence intensity 2 m downstream of the seeding rakes is reported with 1.9 % by the authors [8]. A nominal tracer is 300 µm in diameter.

Tab. 1 Seeding systems for HFSB tracer particles

	4W – HFSB Rake	10W – HFSB Rake
Number of HFSB nozzles	80	200
Number of wings	4	10
Wing pitch (horizontal)	5 cm	5 cm
Nozzle pitch (vertical)	2.5 cm	5 cm

Two CVV systems are employed in the experimental studies. Both systems rely on four CMOS imagers installed in a compact fashion, integrated with an optical fiber transmitting light (λ = 527 nm) generated by a Quantronix Darwin-Duo Nd-YLF laser (2 × 25 mJ pulse energy at 1 kHz). The first CVV system features a square camera arrangement in a prismatic housing (Fig. 2– left) as used by [8, 9 & 16], while the updated system arranges the cameras in a diamond shape, increasing the tomographic aperture in the horizontal plane and allowing for a more aerodynamically shaped housing (Fig. 2 – right). The second CVV probe houses faster cameras and it is utilized in the sphere flow experiment (Sec. 3.1). Technical specifications of the two CVV systems are summarized in Tab. 2.

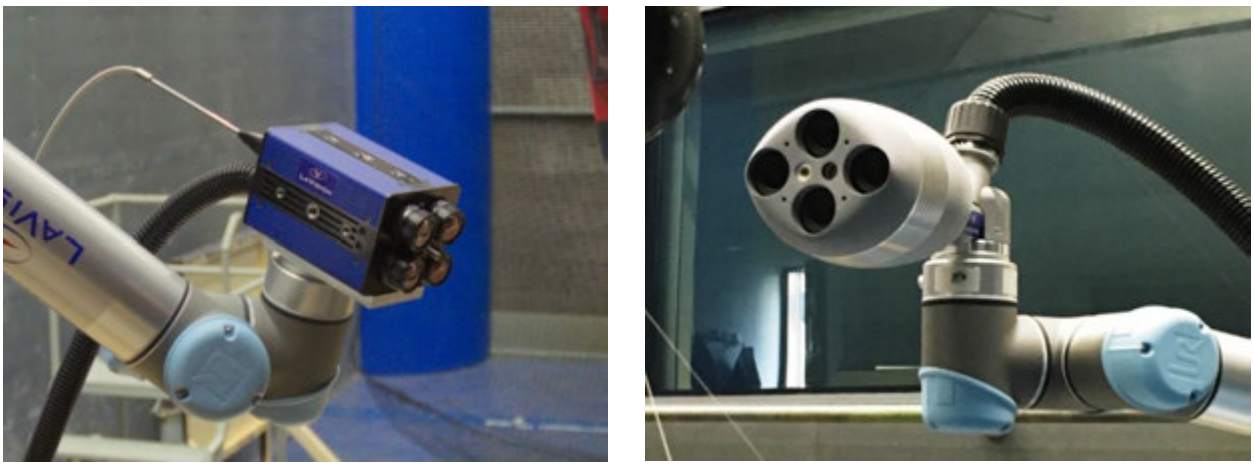

Fig. 2 CVV probe V1 with square camera arrangement (left) and V2 with aerodynamic housing and diamond lens arrangement (right)

Tab. 2 Technical specifications CVV probes

			MiniShaker S	MiniShaker Aero
Housing			Prismatic	Oval
Optics	Focal length	f_i	4 mm	4 mm
	Numerical aperture	$f_\#$	8	11
Imaging	Tomographic aperture (at z_0 = 40 cm)	β	4°	8° horizontal 4° vertical
	Active sensor	$S_x \times S_y$	640 × 475 px	640 × 475 px
	Pixel pitch	Δ_{px}	4.8 µm	4.8 µm
	Magnification (at z_0 = 40 cm)	M	0.01	0.01
	Bit depth	b	10	10
	Acquisition frequency	f	758 Hz	821 Hz

The CVV systems are calibrated by a combination of a geometrical calibration using a conventional pinhole model (Soloff et al. 1997 [20]) and a subsequent volume self-calibration (Wieneke 2008 [23]).

3.1 Sphere flow

The first experiment captures the flow around a sphere of 10 cm diameter at 12 m/s freestream velocity yielding a sub-critical Reynolds number of $Re_d = 7.9 \times 10^4$ (Achenbach, 1972 [1]). The sphere features a static pressure tap in the horizontal symmetry plane. The pressure tap orifice is 0.4 mm in diameter. The pressure tap hose and a supporting steel rod pass through a 8 mm thick, 30 mm chord and 10 cm span airfoil-shaped support structure which is further connected to a 0.5 m long steel rod (d = 10 mm) that connects the test object to the ground. The sphere can be rotated around the vertical axis, allowing for multiple pressure tap measurements in the horizontal symmetry plane, while the support remains stationary.

The exact pressure tap location is determined through tomographic imaging with the CVV probe and reconstruction of the pressure tap location by means of iterative particle reconstruction (IPR, Wieneke 2013 [24]). A set of tensioning steel wires (d = 0.3 mm) is attached to the support to suppress model vibrations induced by the flow.

The CVV system (LaVision MiniShaker Aero) is installed on a collaborative robotic arm (Universal Robots UR5) alongside the sphere model. An illustration of the setup with the 10W – HFSB rake installed at the contraction exit is given in Fig. 3.

The CVV probe is placed at approximately 40 cm distance to the sphere center, viewing perpendicular to the freestream direction. The probe is translated in the streamwise direction by means of the collaborative robotic arm to acquire flow data up- and downstream of the sphere. Images are taken at a frequency of 821 Hz, yielding a particle displacement of 14.6 mm in the freestream respectively an equivalent displacement of 27 px on the camera sensor at a nominal measurement distance of z = 40 cm. The observed particle image density is about N_p = 0.01 ppp. An instantaneous image of a typical measurement is presented in Fig. 4.

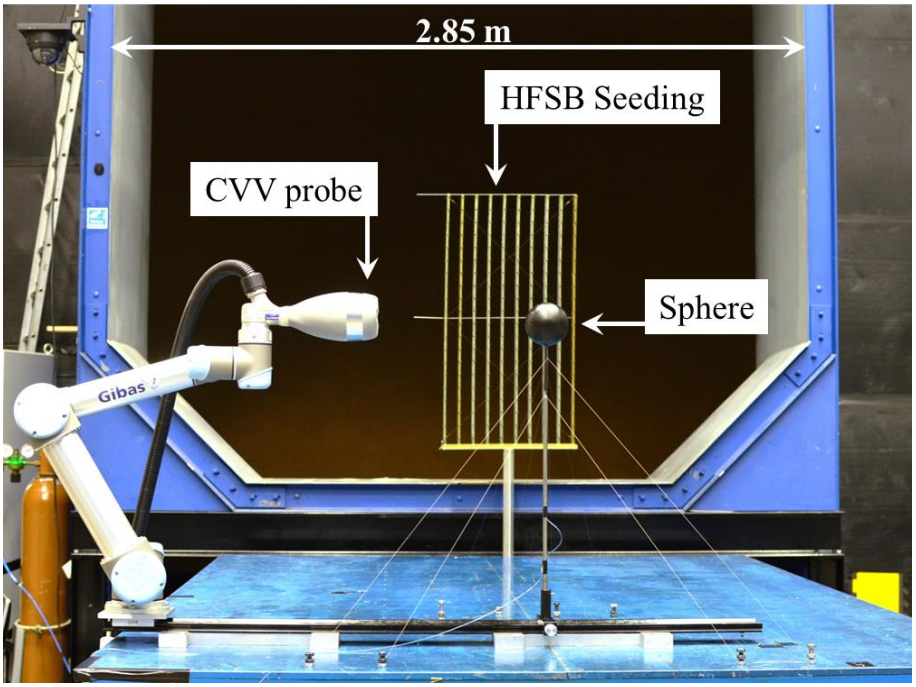

Fig. 3 Experimental setup for the sphere flow experiment in OJF

Raw PIV images are first pre-processed with a Gaussian smoothing operator on a 5×5 px kernel followed by a Butterworth high-pass frequency filter (Sciacchitano and Scarano 2014 [18]) using a 7-image filter length. The temporal high pass filter efficiently eliminates the laser reflections on the sphere and in the background as can be appreciated from Fig. 4. The CVV images are subsequently processed by the Lagrangian particle tracking algorithm Shake-the-Box (STB) as discussed in Sec. 2.2. The measurement volume of an individual measurement is on the order of 10 liters.

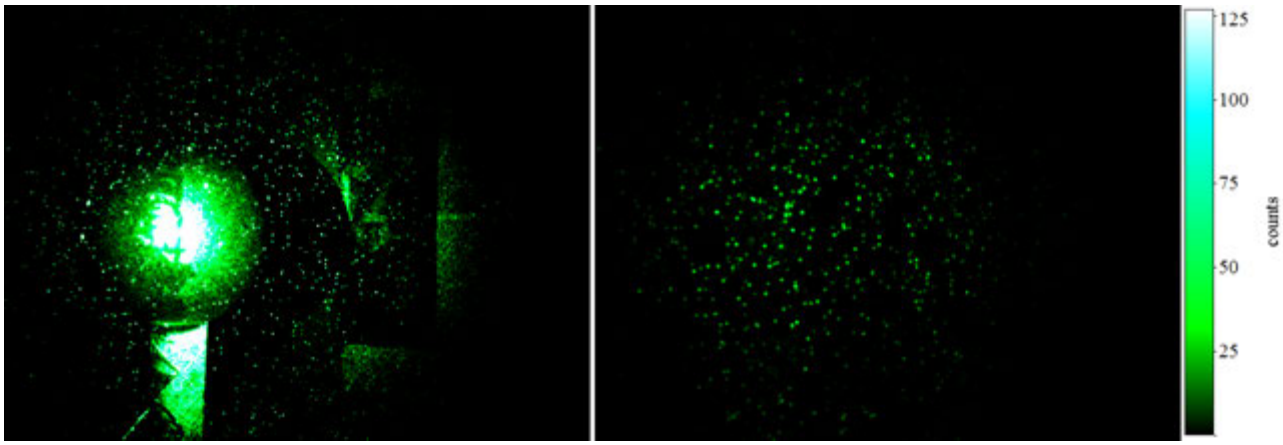

Fig. 4 Instantaneous particle image. Raw image (left) along with pre-processed image (right).

3.2 Cyclist investigation

An additively manufactured full-scale replica of the 2017 time-trial world champion Tom Dumoulin (van Tubergen et al. 2017 [22]) is installed on a Giant Trinity time-trial bike in the OJF. The layout of the experimental setup is presented in Fig. 5. A detailed description of the measurement setup is given in another work of the authors [8].

PTV images are acquired over 450 subsequent measurements of 5,000 frames at 758 Hz each. As described in Sec. 2.2 Lagrangian particle tracking (Shake-the-Box, Schanz et al. 2016 [15]) provides the means of evaluating particle velocities. The unstructured velocity data is subsequently temporally and spatially averaged to a Cartesian grid featuring 400×320×140 cubic cells of 8 cm^3 with 75% overlap resulting in a vector spacing of 5 mm on a measurement domain of 2,000×1,600×700 mm^3.

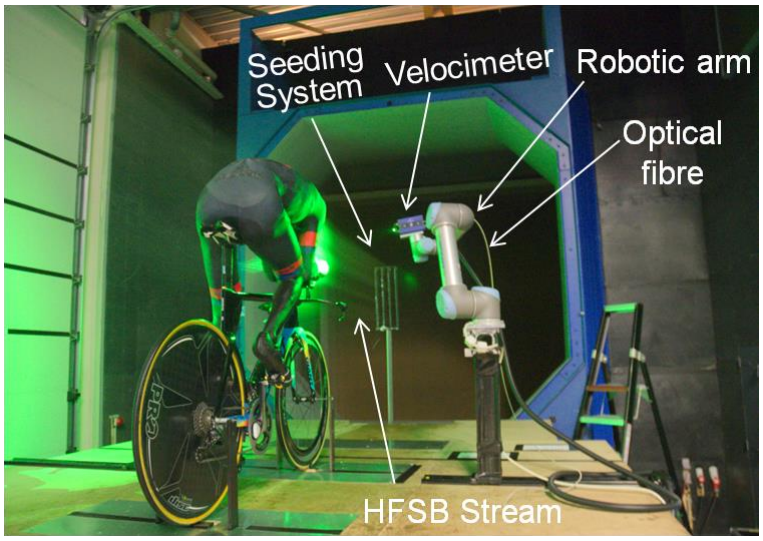

Fig. 5 Experimental setup of the cyclist experiment with full-scale model, seeding generator and robotic PIV system. Figure reproduced from [8].

4 Results

An assessment of the pressure mapping models is presented for the sphere flow experiment, involving sensitivity analysis of velocity and pressure field with respect to spatial resolution. Subsequently, the most suitable approach is selected and applied to the cyclist data, evaluating the pressure on the athlete.

4.1 Sphere flow

The measured velocity field in the horizontal symmetry plane is presented together with the pressure field in Fig. 6 super-positioned with contours of the potential flow solution for the upstream flow region.

The single-sided measurement contains a shadowed region at the side of the sphere (positive y). The velocity contour in Fig. 6 – left shows a good match with potential flow data upstream of the sphere. Further, a clear acceleration is observed at $\theta = 90°$, arising from the blockage of the sphere and the curvature of the surface. Downstream of the high momentum flow, the flow separates at $\theta \approx 105°$, which is shown by a strong velocity gradient across the shear layer in the sphere wake.

Fig. 6 – right shows the pressure field that is obtained from the velocity field measurement shown in Fig. 6 – left through application of the Poisson equation (eq. 1). The Dirichlet condition is imposed upstream of the sphere at $x/R = -4$, assuming potential flow conditions. Again, the trend upstream of the sphere matches well with the potential flow solution, featuring a rise in pressure towards the stagnation point as well as a reduction in pressure towards the maximum thickness point ($\theta = 90°$). The sphere wake features a low pressure region, with two minima at approx. ($x/R = 1.5$, $y/R = |0.6|$). These minima are connected by a torus like structure when visualized in 3D, as shown in Fig. 7.

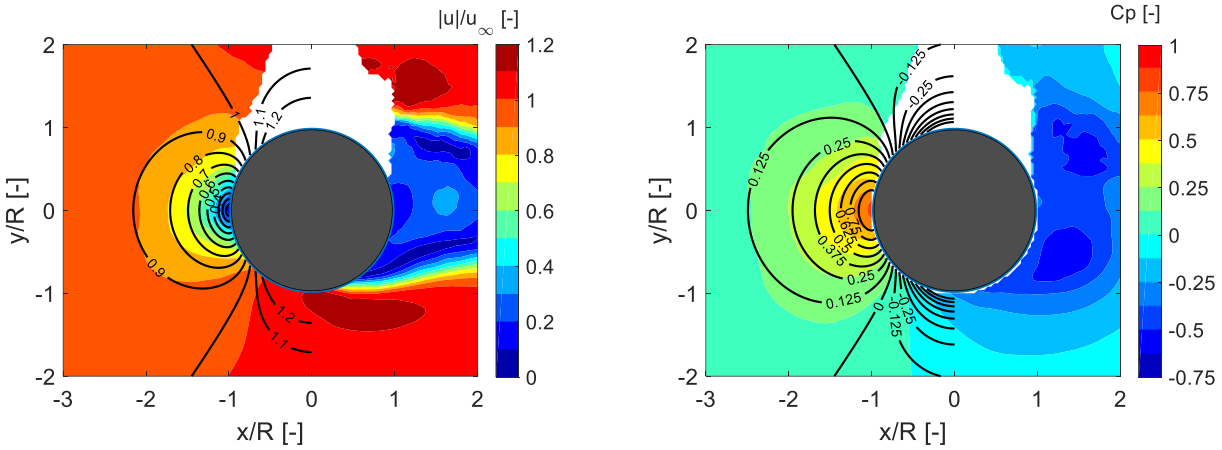

Fig. 6 Normalized velocity and pressure field in the *xy*-plane at a linear bin-size of l_V = 15 mm.

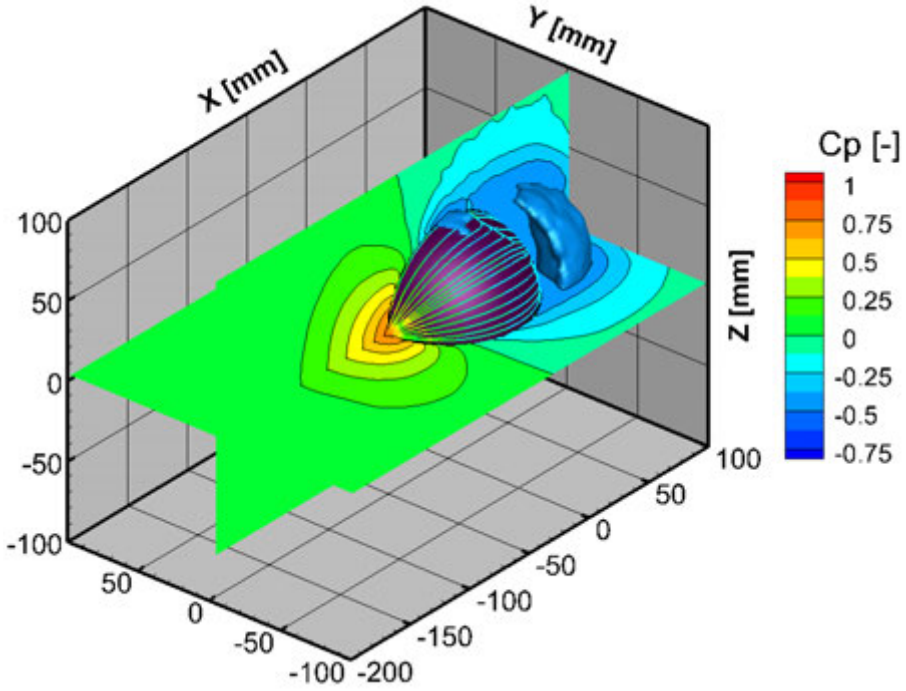

Fig. 7 C_p contours in horizontal and vertical symmetry planes along with iso-surface of C_p = -0.5. Surface friction lines on sphere colored by C_p.

The measurement data is compared to the potential flow solution in more detail along the stagnation line in Fig. 8. The velocity gradient near stagnation is high, and thus, it can be anticipated that any error in the measurement data, arising from spatial averaging will be pronounced near the sphere's stagnation point.

Well upstream of the sphere the measurement data matches with the potential flow solution, whereas close to the object the flow velocity is overestimated by the PTV measurement. The overestimation in velocity is an artifact of the spatial averaging. Fig. 8 – right indicates that the error in the velocity measurement near the object surface can be limited by selecting higher spatial resolution. For the two extreme cases of a linear bin size of l_V = 50 mm, the velocity error at stagnation is as high as 50 %,

which can be improved to less than 10% when reducing l_V to 5 mm. Refining the measurement grid typically comes at the cost of acquiring and processing more PTV data.

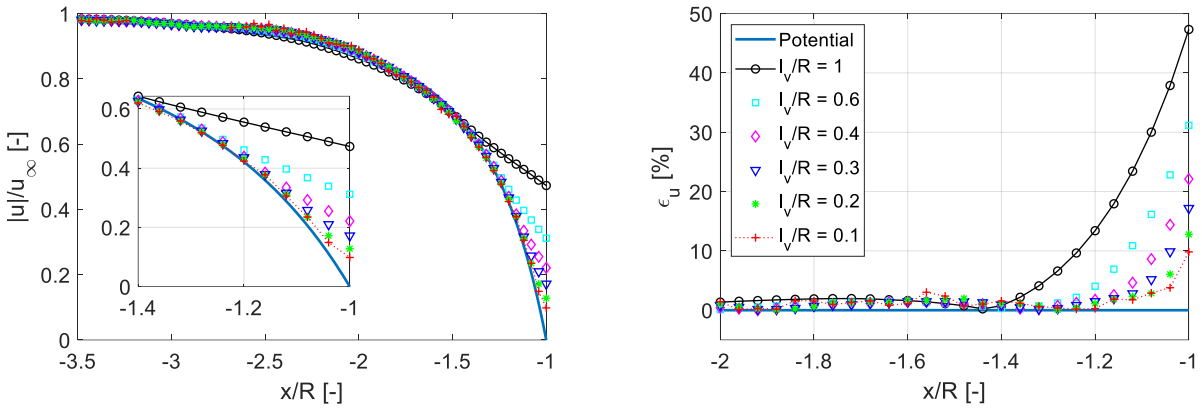

Fig. 8 Normalized velocity profile along sphere stagnation line for varying averaging volume sizes (left) and corresponding error plot (right).

The sensitivity of the velocity measurement with respect to spatial resolution l_V/R is quantified in terms of the measurement error ε_u with respect to the freestream velocity u_0

$$\epsilon_u = \frac{u_m - u_{pot}}{u_0} \tag{5}$$

There is a clear trend that the velocity gradient is better represented as the grid resolution is refined, see Fig. 8. Due to error propagation from the velocity measurement into the pressure field, it is of utmost importance to accurately represent the velocity field and thus, to attain a sufficient spatial resolution of the measurement grid. This requires a balance between desired resolution and the amount of data which is acquired.

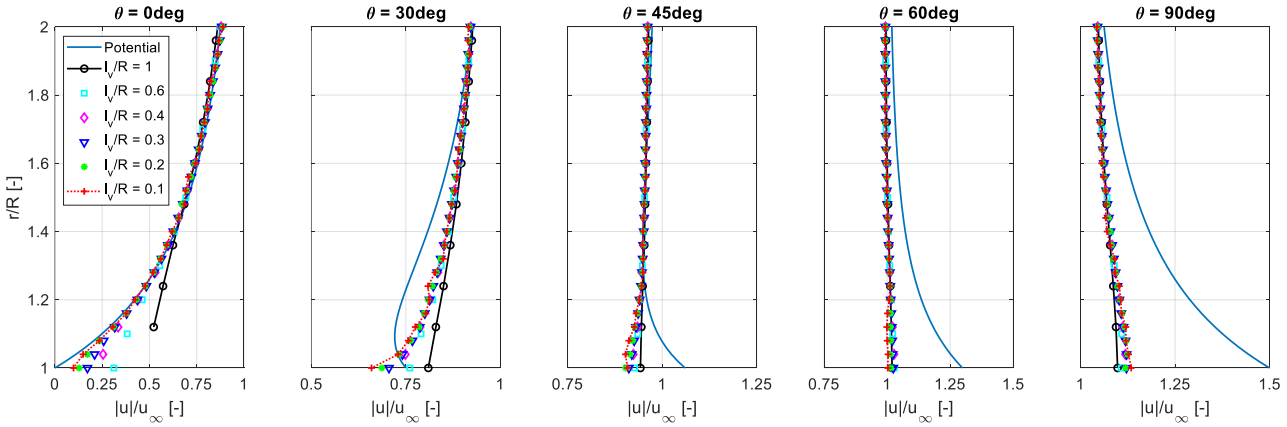

Fig. 9 Normalized velocity profiles for different azimuth angles and spatial resolution.

Next to the stagnation line, a selection of velocity profiles for varying azimuth angles is presented in Fig. 9 along with the potential flow solution. The PTV measurement and the potential flow solution match best for large r/R. Approaching the object surface, the theoretical solution and the measurement data deviate increasingly with azimuth. For large θ (> 45°) this may be attributed to the fact that the potential flow solution is not representative of the actual flow anymore. Interestingly, in this regime

(45°≤ θ ≤ 90°) the velocity profile presented by the PTV measurement is rather flat, and thus, the differences recorded between the fine and the coarse grids are relatively small. For moderate azimuth (θ = 30°) where the velocity gradient is more appreciable, the effect of spatial resolution is comparable to the analysis along the stagnation line presented above: the higher the spatial resolution, the steeper the measured velocity gradient near the sphere surface. Noticeably, the velocity profiles for the PTV measurements at θ = 30° are monotonically increasing, whereas the potential flow solution indicates a local minimum at r/R = 1.1.

Considering solely spatial resolution, the finest attainable resolution will provide the most accurate results in terms of velocities and pressures along the stagnation line. The experimentalist shall recall however, that the uncertainty of the mean velocity measurement will rise, as the bin size and consequently the number of samples N per bin is reduced.

$$\epsilon = \frac{k\sigma_u}{\sqrt{N}} \tag{6}$$

Thus, to maintain the measurement uncertainty at a desirable level, attention is to be paid to separated flow regions, where velocity fluctuations σ_u are high, while the number of particles N which is tracked is typically lower as compared to laminar flow regions. For the present dataset, a linear bin size of l_V = 15 mm yields N_{avg} = 1,000 particles per bin which is considered to yield a sufficient uncertainty level of the time-averaged flow quantities. Therefore, the remainder of the analysis is executed for a constant bin size of l_V = 15 mm.

Given that the velocity measurement is accurate only up to a finite distance of the object surface, flow quantities at the object surface may be estimated by the application of suitable models. As indicated in the introduction, a linear extrapolation, a quadratic interpolation under the application of von Neumann boundary conditions and lastly, a stagnation model approach are employed for the surface pressure evaluation. The three models are again compared to the potential flow solution upstream of the sphere, along the stagnation line. Additionally the pressure is computed from Bernoulli's equation assuming a constant total pressure equal to the stagnation pressure and taking the measured velocity field as input. Then,

$$p_{Ber} = 1 - \left(\frac{|u|}{u_\infty}\right)^2 \tag{7}$$

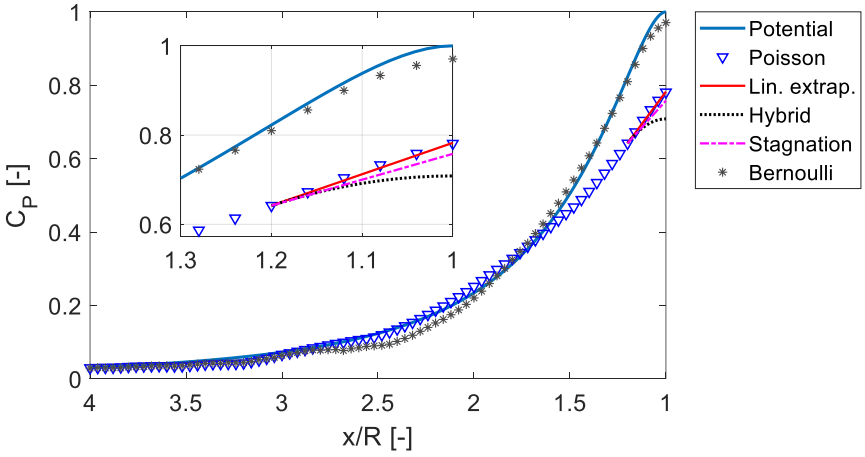

Fig. 10 Pressure coefficient C_P along sphere stagnation line, comparing different surface-pressure mapping models at a constant mapping distance of 10 mm.

Fig. 10 shows that the pressure along the stagnation line is matched well far upstream of the sphere. Close to the stagnation point, where the velocity is found to be overestimated by the PTV measurement, the measured pressure is consequently underestimated. The best estimation of surface pressure is attained by application of Bernoulli's equation using the velocity measurement directly. The solution of the Poisson solver and the linear extrapolation model yield a stagnation pressure of C_P = 0.79 only and thus, they cause an error of 21% in C_P. The stagnation- and the hybrid model further lower the estimated pressure in the stagnation point, and they can therefore be considered to perform worse.

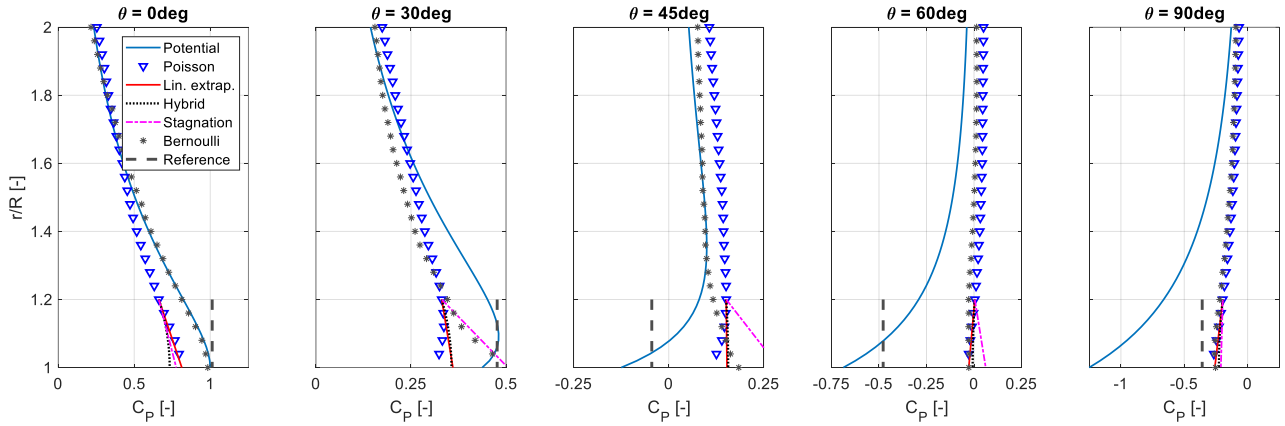

Fig. 11 Pressure coefficient C_P for different azimuth, comparing the selected surface pressure mapping models at a constant mapping distance of 10 mm.

Next to the comparison along the stagnation line, the performance of the extrapolation models is further compared for different azimuthal positions (Fig. 11). For $\theta = 30°$, the stagnation model provides a good correction and matches with the pressure tap measurement to within 0.03 C_P. The model does however fail for greater azimuth, significantly overestimating the surface pressure at 45°. While the application of Bernoulli's equation produces good results for small and moderate azimuth ($\theta \leq 30°$) it deviates clearly beyond $\theta = 30°$. The linear extrapolation and the hybrid model perform similar, but their relatively small corrections do not seem to improve the direct solution from the Poisson solver significantly.

Fig. 12 instead compares only the estimated surface pressures over the sphere in the horizontal symmetry plane. The data is compared to the reference pressure values provided by the pressure tapping. For small azimuth, application of Bernoulli's equation under the assumption of constant total pressure provides best results. The model fails in the region of separated flow however, where the assumption of constant total pressure does not hold true.

The pressure tap records a suction peak at $\theta = 70°$, which is well in line with literature (Achenbach, 1972 [1]). None of the tested models is able to reproduce this suction peak. Instead, all models show a gradual reduction in pressure with azimuth, up to $\theta = 120°$. Note, that previous studies by other groups (e.g. Auteri et al. (2015) [3]; Ragni et al. (2009) [11]) show similar behaviour in the sense that local pressure minima are not well captured by evaluation of the pressure field through PIV.

Beyond the suction peak, the pressure in the wake is estimated comparably well, staying within 0.1 C_P of the pressure tap measurements. In fact, the uncorrected result from the Poisson solver provides the surface pressure closest to the tapping measurements in the wake and therefore, no correction model will be applied to the pressure field evaluation of the cyclist data in the following section.

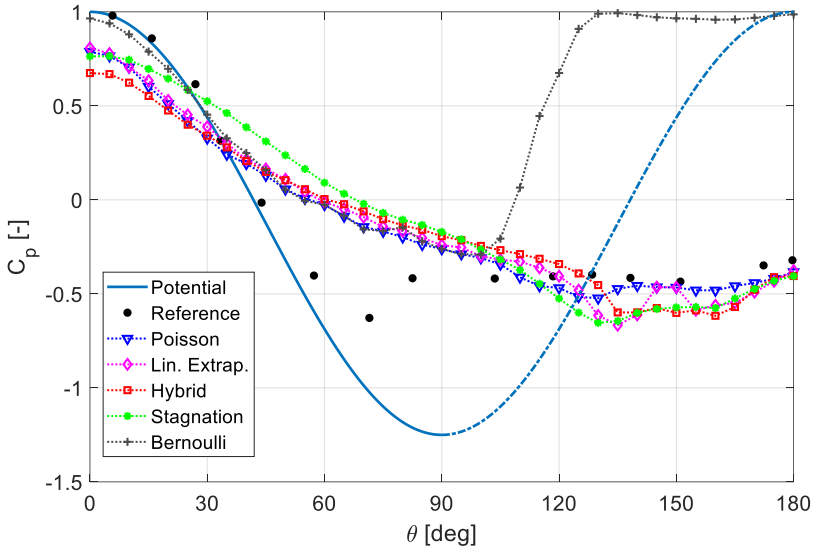

Fig. 12 Azimuthal pressure coefficient distribution in the *xy*-plane for selected mapping models at constant mapping distance of 10 mm. Reference measurement provided by pressure tapping.

4.2 Cyclist

The time-averaged velocity field around the full-scale cyclist replica of Tom Dumoulin at 14 m/s free-stream velocity is analyzed in a previous work of the authors [8]. Some key findings are summarized to connect to the pressure field evaluation in this work.

Fig. 13 shows the streamwise velocity contours in the median plane, alongside a visualization of the dominant wake structures by means of an iso-surface at 50% free-stream velocity. The velocity contour plane indicates stagnating flow at the rider's helmet and hands. Over the curved upper back a flow acceleration is observed which peaks at the highest point of the back. Further downstream, the adverse pressure gradient results in a flow deceleration which finally causes a flow separation at the lower back. The wake visualization in Fig. 13 – left indicates strong velocity deficits downstream of the upper arm and the stretched leg. Furthermore, the flow deceleration upstream of the stretched leg is captured indicating stagnation of the flow.

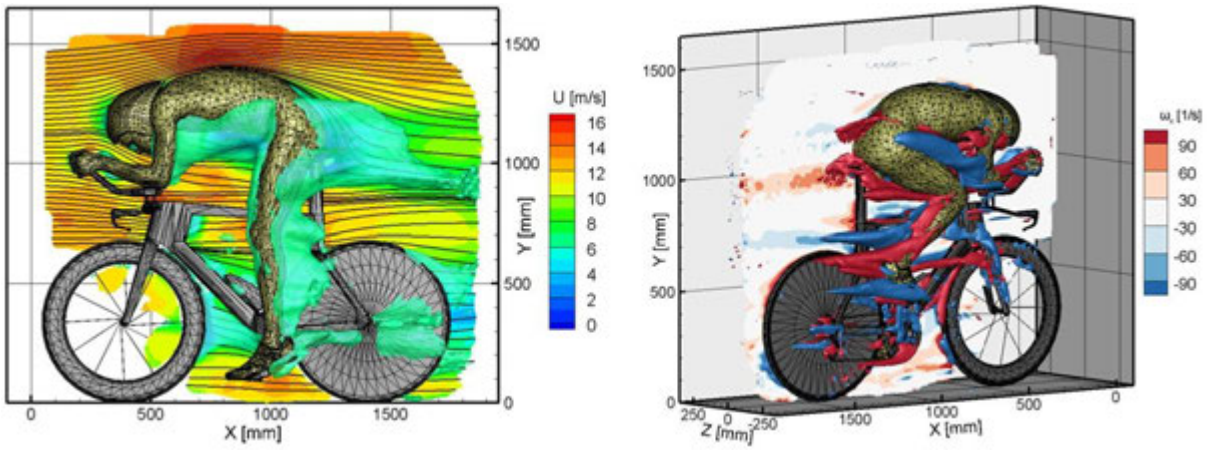

Fig. 13 Time-averaged velocity (left) and vorticity (right) field of the full-scale cyclist measurement. Contour-planes in the *xy*-plane, iso-surfaces indicate 50% free-stream velocity (left) respectively streamwise vorticity ω_x = |100| Hz (right). Figures reproduced from [8].

Iso-surfaces of streamwise vorticity illustrated in Fig. 13 –right highlight the presence of a multitude of (counter-rotating) vortices emanating from the cyclist's body. A major clockwise rotating (blue) vortex is developing at the right arm, facing an upward trajectory along the right upper leg. Inside the thigh, a counter-clockwise rotating (red) vortex is observed, which matches well with observations in literature (Crouch et al, 2016 [5]; Spoelstra et al. 2018 [21]). On the lower leg respectively the rider's foot, a quadrupole of counter-rotating vortices emerges which interact as they travel downstream.

For analysis of the near-surface flow topology, velocity and pressure are evaluated on a 5 mm dilated surface from the cyclists body, see Fig. 14 – 16.

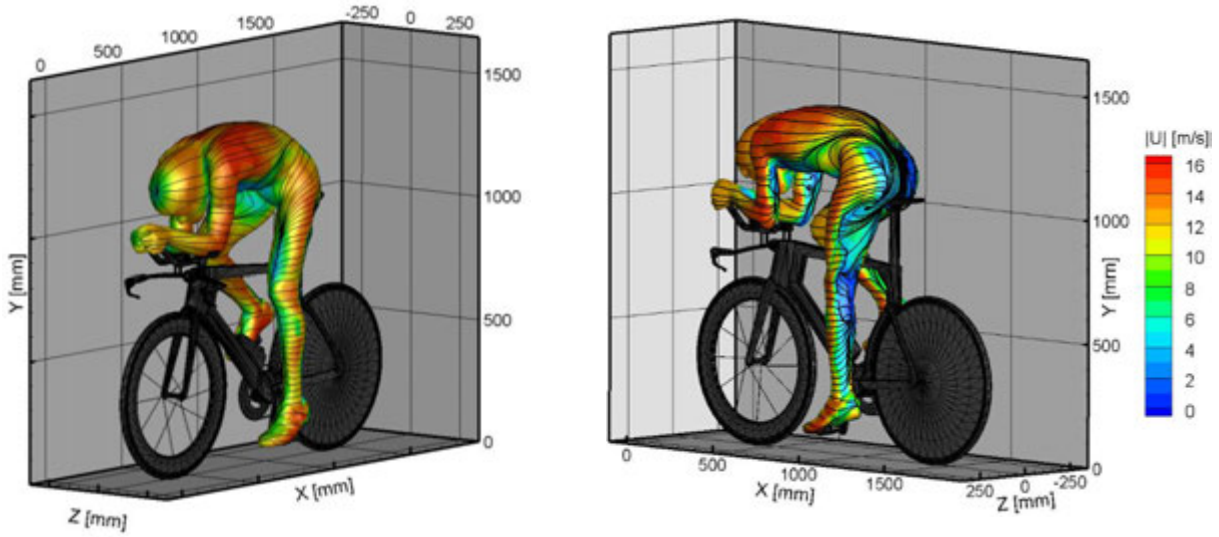

Fig. 14 Velocity magnitude evaluated at a 5 mm dilated surface along with surface friction lines.

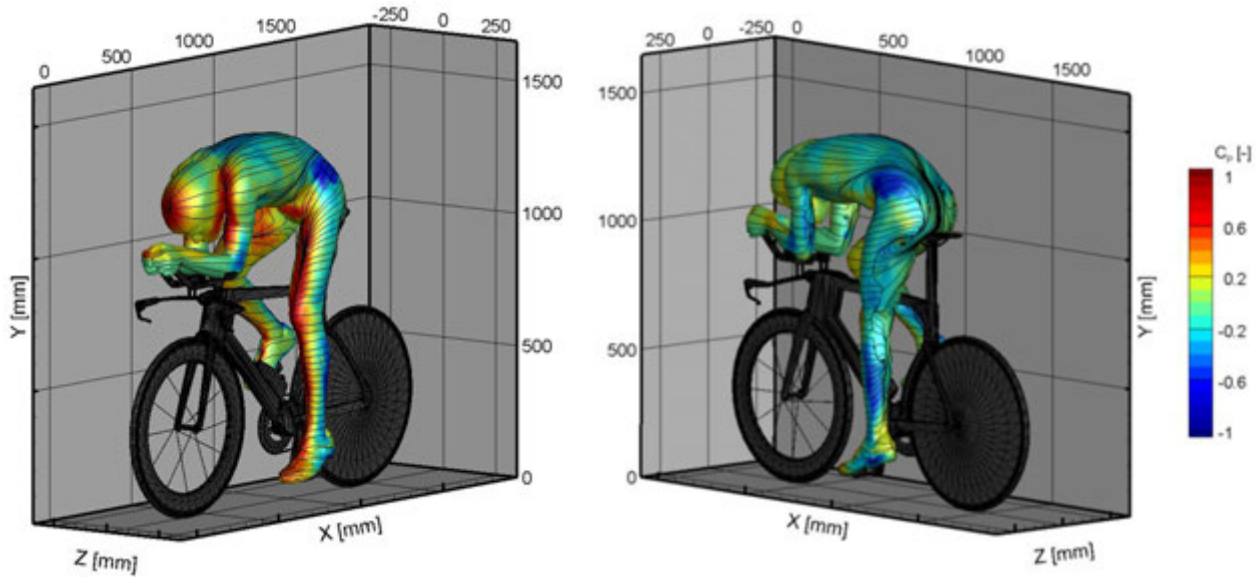

Fig. 15 Pressure coefficient C_P evaluated at a 5 mm dilated surface along with surface friction lines

The surface-friction lines in Fig. 14 show a stagnation point on the cyclists helmet, as well as a stagnation line along the forward upper arm and the front face of the stretched leg. Further, a strong

upwash component is seen at the left hip. The lower back and the back face of the stretched leg are instead characterized by low velocity magnitude and flow recirculation.

The analysis of the sphere flow shows that the proposed correction models do not suffice to improve the surface pressure estimation across the different flow regimes experienced by the sphere. As such the pressure visualizations of the full-scale cyclist measurement feature the direct Poisson solution, evaluated on a 5 mm dilated surface from the athlete's body.

Comparing the surface-friction lines with the surface pressure visualizations in Fig. 15 in a qualitative manner, the above mentioned stagnation point on the helmet as well as the stagnation lines along upper arm and stretched legs correlate well with the high pressure measured in exactly these regions. The acceleration over the curved upper back results in a low pressure region. Suction peaks can be appreciated near the left elbow, the outside part of the lower left leg and the left hip where a clear upward flow direction has been observed.

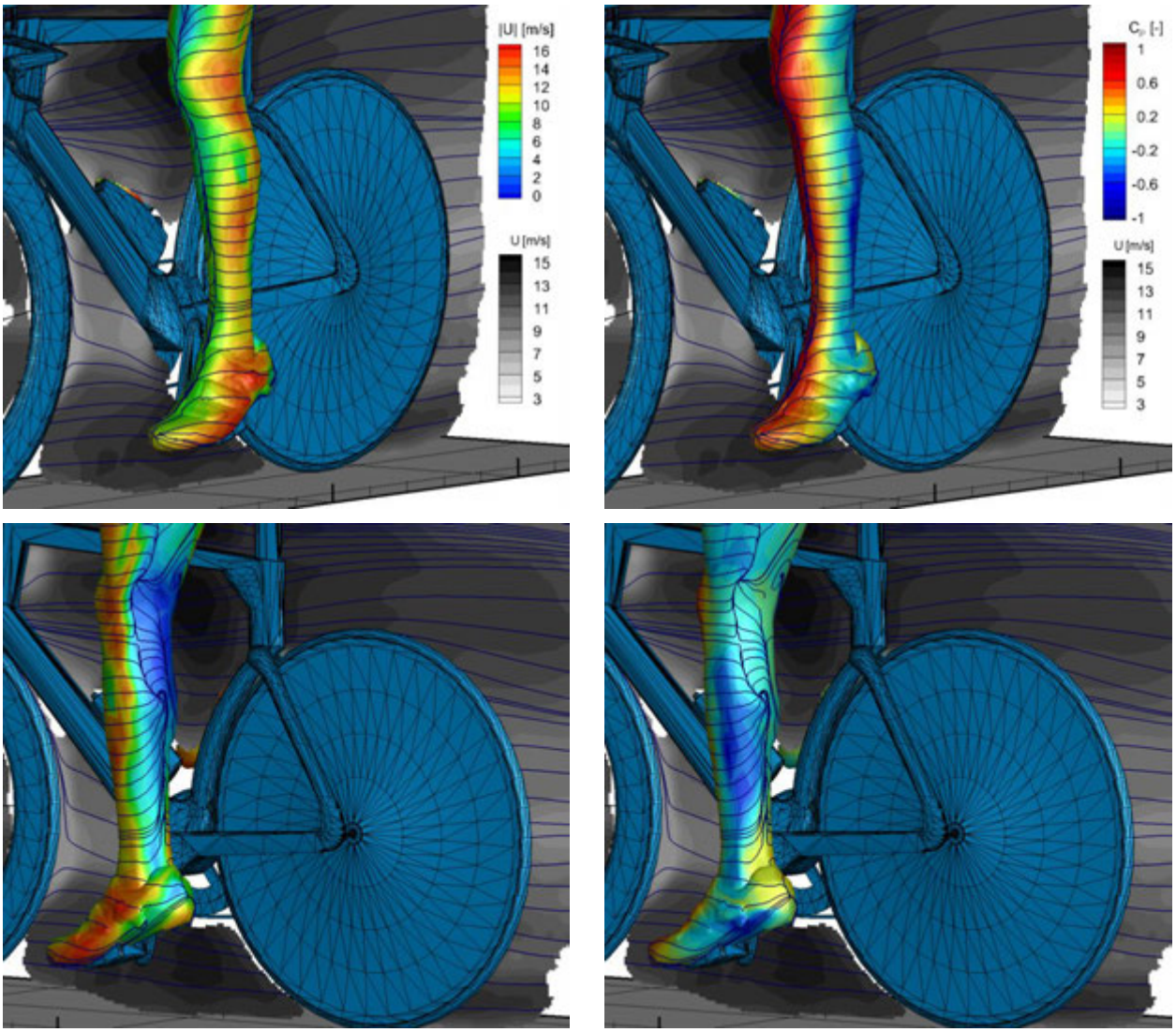

Fig. 16 Contours of velocity magnitude (left) and corresponding pressure distribution (right) for the stretched left leg on a 5 mm dilated surface.

Zooming in onto the lower left leg (Fig. 16) and comparing velocity magnitude to C_P, a number of observations are made: the stagnation line along the forward face of the stretched leg connects the two stagnation points found on the tip of the shoe and the cyclist's knee. The region of high C_P follows the path drawn by the stagnation line between these points. As the flow accelerates around the leg and the shoe, the pressure coefficient rapidly drops resulting in a suction on the side of the leg respectively the shoe.

The rear view onto the lower leg in Fig. 16 – bottom shows a large separation region on the upper part of the calf and above, whereas on the lower calf the flow appears to stay attached longer. It is hypothesized that this is a result of the counter-rotating vortices developing around the shoe similar to the vortex pattern for the right leg shown in Fig. 16 – right. It is seen that the suction peak is stronger on the lower part of the leg where the separation is smaller.

5 Conclusions and recommendations

An attempt is made to evaluate the surface pressure on large-scale and complex objects from robotic volumetric PTV data. A stumbling block in the surface-pressure evaluation from 3D time-averaged PTV data is its finite spatial resolution, yielding measurements at a finite distance to the object surface as well as truncation errors in regions of high velocity gradients. Three extrapolation models are proposed and tested to map the field pressure provided by the solution of the Poisson equation onto the surface. It is found that none of the tested methods achieves a significant improvement in the surface pressure estimation when comparing to pressure tap data on a sphere. It is further shown that the accuracy of the velocity field measurement increases with higher spatial resolution, in particular in areas where gradients are large. Higher spatial resolution may be achieved by smart averaging techniques as proposed by Agüera et al. (2016) [2], by the application of anisotropic averaging volumes based on the directionality of the observed velocity gradients, or simply by acquisition of more PTV data. Furthermore, improvements in the Poisson solution are expected by more accurate treatment of the boundary conditions along object surfaces, which are currently handled by a uniform Cartesian mesh but which may be modeled better by integration of a surface mesh in the measurement domain.

References

[1] Achenbach E. Experiments on the flow past spheres at very high Reynolds numbers. *Journal of Fluid Mechanics*, Vol. 54, No. 3, pp. 565-575, 1972.

[2] Agüera N, Cafiero G, Astarita T and Discetti S. Ensemble 3D PTV for high resolution turbulent statistics. *Measurement Science and Technology*, Vol. 27, No. 12, 2016.

[3] Auteri F, Carini M, Zagaglia D, Montagnani D, Gibertini G, Merz CB and Zanotti A. A novel approach for reconstructing pressure from PIV velocity measurements. *Experiments in Fluids*. Vol 56, No. 45, 2015.

[4] Caridi GCA, Ragni D, Sciacchitano A and Scarano F. HFSB-seeding for large-scale tomographic PIV in wind tunnels. *Experiments in Fluids*. Vol. 57, No. 12, 2016.

[5] Crouch TN, Burton D, Thompson MC, Brown NAT and Sheridan. Dynamic leg-motion and its effect on the aerodynamic performance of cyclists. *Journal of Fluids and Structures*. Vol. 65, pp. 121-137, 2016.

[6] Ebbers T and Farnebäck G. Improving computation of cardiovascular relative pressure fields from velocity MRI. *Journal of Magnetic Resonance Imaging*. Vol. 30, No. 1, pp. 54-61, 2009.

[7] Faleiros DE, Tuinstra M, Sciacchitano A and Scarano F. Helium-filled soap bubbles tracing fidelity in wall-bounded turbulence. *Experiments in Fluids*. Vol. 59, No. 3, 2018.

[8] Jux C, Sciacchitano A, Schneiders JFG and Scarano F. Robotic volumetric PIV of a full-scale cyclist. *Experiments in Fluids*, Vol. 59, No. 4, 2018.

[9] Martínez Gallar B, van Oudheusden B, Sciacchitano A and Karásek M. Large-scale flow visualization of a flapping-wing micro air vehicle. *In proceedings of International Symposium on Flow Visualization ISFV 18*, Zurich, Switzerland, 26-29 June 2018.

[10] van Oudheusden BW. PIV-based pressure measurement. *Measurement Science and Technology*. Vol 24, No 3, 2013.

[11] Ragni D, Ashok A, van Oudheusden BW and Scarano F. Surface pressure and aerodynamic loads determination of a transonic airfoil based on particle image velocimetry. *Measurement Science and Technology*. Vol. 20, No. 7, 2009.

[12] Ragni D, van Oudheusden BW and Scarano F. 3D pressure imaging of an aircraft propeller blade-tip flow by phase-locked stereoscopic PIV. *Experiments in Fluids*. Vol. 52, No. 2, pp. 463-477, 2012.

[13] Rius Vidales AF. Air-wake flow dynamics on a simplified frigate shape: an experimental study by large-scale tomographic PTV. *TU Delft MSc thesis*. 2016

[14] Scarano F, Ghaemi S, Caridi GCA, Bosbach J, Dierksheide U and Sciacchitano A. On the use of helium-filled soap bubbles for large-scale tomographic PIV in wind tunnel experiments. *Experiments in Fluids*. Vol. 56, No 2, 2015.

[15] Schanz D, Gesemann D and Schröder A. Shake-The-Box: Lagrangian particle tracking at high particle image densities. *Experiments in Fluids*. Vol 57, No. 5, 2016.

[16] Schneiders JFG, Scarano F, Jux C and Sciacchitano A. Coaxial volumetric velocimetry. *Measurement Science and Technology*, Vol. 29, No. 6, 2018.

[17] Schneiders JFG, Caridi GCA, Sciacchitano A and Scarano F. Large-scale volumetric pressure from tomographic PTV with HFSB tracers. *Experiments in Fluids*. Vol. 57, No. 11, 2016.

[18] Sciacchitano A and Scarano F. Elimination of PIV light reflections via a temporal high pass filter. *Measurement Science and Technology*. Vol 25, No. 8, 2014.

[19] Sciacchitano A, Terra W and Shah YH. Aerodynamic drag determination of a full-scale cyclist mannequin from large-scale PTV measurements. *In proceedings of the 19th international symposium on applications of laser and imaging techniques to fluid mechanics*, Lisbon, Portugal, 16-19 July 2018

[20] Soloff SM, Adrian RJ and Liu ZC. Distortion compensation for generalized stereoscopic particle image velocimetry. *Measurement Science and Technology*. Vol 8, No 12, 1997.

[21] Spoelstra A, de Martino Norante L, Terra W, Sciacchitano A and Scarano F. An assessment of the ring of fire approach for indoor and outdoor on-site sports aerodynamic investigation. *In proceedings of the 19th international symposium on applications of laser and imaging techniques to fluid mechanics*, Lisbon, Portugal, 16-19 July 2018

[22] van Tubergen J, Verlinden J, Stroober M and Baldewsing R. Suited for performance: Fast full-scale replica of athlete with FDM. *In proceedings of the 1st Annual ACM Symposium on Computational Fabrication*, Cambridge, MA, USA, 12–13 June 2017

[23] Wieneke B. Volume self-calibration for 3D particle image velocimetry. *Experiments in Fluids*. Vol. 45, No 4, 2008.

[24] Wieneke B. Iterative reconstruction of volumetric particle distribution. *Measurement Science and Technology*. Vol 24, No. 2, 2013.

Copyright Statement